
Article:
Ge, R., Cumming, D.J. and Smith, R.M. orcid.org/0000-0003-2340-0042 (2022) Discrete element method (DEM) analysis of lithium ion battery electrode structures from X-ray tomography-the effect of calendering conditions. Powder Technology, 403. 117366. ISSN 0032-5910

https://doi.org/10.1016/j.powtec.2022.117366

Powder Technology 403 (2022) 117366

Contents lists available at ScienceDirect

Powder Technology

journal homepage: www.elsevier.com/locate/powtec

Discrete element method (DEM) analysis of lithium ion battery electrode structures from X-ray tomography-the effect of calendering conditions

Ruihuan Ge [a,b], Denis J. Cumming [a,b], Rachel M. Smith [a,b,*]

[a] Department of Chemical and Biological Engineering, The University of Sheffield, Sheffield S10 2TN, UK
[b] The Faraday Institution, Quad One, Harwell Science and Innovation Campus, Didcot OX11 0RA, UK

ARTICLE INFO

Article history:
Received 22 December 2021
Received in revised form 25 March 2022
Accepted 3 April 2022
Available online 14 April 2022

Keywords:
Discrete Element Method (DEM)
Lithium-ion battery
Calendering
X-ray tomography

ABSTRACT

Calendering is an essential process step to manufacture electrodes for lithium-ion batteries. The relationship between the various component material properties and calendering conditions has a large impact on the battery performance. In this work, Discrete Element Method (DEM) was used to investigate the electrode structure evolution under different calendering conditions. The initial positions of active material (AM) particles were obtained from an uncalendered electrode microstructure characterised experimentally by X-ray tomography and then imported to DEM simulations. Simulated structures under different processing conditions were obtained by compression tests in DEM. The Edinburgh elasto-plastic adhesive (EEPA) model and bond model were used to describe the mechanical response of AM particles and binder phase during compression. Detailed stress and structural evolutions at microscopic scale were further analysed. For the first time, the results demonstrate a promising way to predict and design battery electrode structures by combining X-ray tomography and DEM analysis.

1. Introduction

Lithium-ion batteries play a crucial role in transforming the energy storage field. They have been widely used in different fields from portable electronics to electrical vehicles [1]. To improve battery performance and reduce production costs, substantial efforts have been made to understand the manufacturing process and to optimise the electrode microstructures [2,3]. Calendering is an important step of electrode manufacture, in which the dried electrodes are compressed to control electrode porosity and improve adhesion. Particle connectivity and volumetric energy density are increased during this process. In addition, other performance parameters including mechanical properties and transport properties can also be affected as the electrode structure evolves during calendering [4,5].

Several experimental studies have investigated how calendering affects electrode structure and subsequent battery performance. Meyer et al. [6] systematically investigated the calendering process of graphite anodes and nickel manganese cobalt oxide (NMC) cathodes. The relation between the coating density and circumferential speed, applied line load was studied. An exponential relationship was proposed to describe the compaction force and the measured porosity reduction. The effects of process parameters were further investigated by Schreiner [7]. A machine/material-process-structure model was established to describe the relations between process and structural properties during calendering. Recently, the effect of formulation parameters including active material (AM), carbon additive, binder composition on the calendering processability of cathodes was analysed by Primo et al. [8]. It was found that the electrode mesostructures and the binder phase distribution affects the mechanical properties. It is also important to understand the impact of the calendering process on the electrical properties of lithium ion batteries. Experimental studies have demonstrated that the pore size variations, AM particle deformation and breakage during calendering can affect the electrochemical performance (e.g. electrode resistivity [9], rate capability and long term performance [10,11]).

By using non-destructive imaging techniques such as X-ray computed tomography, 3D microstructures of electrodes can be obtained [12]. Detailed structural information including particle size distribution, binder phase and pore distributions have been analysed [13–15]. The correct characterisation of the microstructures offers important information to fully understand the battery electrode performance. Lu et al. [3] proposed a novel X-ray computed tomography dual-scan superimposition technique to capture the carbon binder domain (CBD) phase within electrode structures. A 3D microstructure-resolved numerical model is further developed to investigate the electrochemical performance of battery electrodes. Furthermore, in situ calendering experiments were performed to investigate the structural evolutions and provide insights to optimise 3D electrode microstructures.

* Corresponding author at: Department of Chemical and Biological Engineering, The University of Sheffield, Sheffield S10 2TN, UK.
E-mail address: rachel.smith@sheffield.ac.uk (R.M. Smith).

https://doi.org/10.1016/j.powtec.2022.117366

The application of numerical modelling has proved to be useful to understand the structure evolutions and battery performance. Discrete Element Method (DEM) models the motion and forces of particles, both of which are important to understand the evolution of structure and stress for granular materials [16,17]. DEM has been widely used in chemical, pharmaceutical and mineral industries to understand different particulate processes. Recently it was applied to understand the microstructures of battery electrodes [18,19]. Using a fabric tensor-based approach, Stershic et al. [20] investigated the evolution of inter-particle contact evolutions of electrodes. The mechanical descriptions of the binder phase were not considered in their research. By purely considering the electrode structure and AM particle size distribution, the DEM simulations could not predict the evolution of inter-particle contacts. Gimenez et al. [19,21] systematically investigated the mechanical and electrical properties of electrodes. In their study, the electrode structures were stochastically generated and the binder phases were described using bond models. Using DEM, they also studied the structural changes and stress evolution during the charging-discharging process. Srivastava et al. [22] proposed a DEM based approach to design the electrode mesostructures. In their work, the initial structures were stochastically generated and the mesostructures were designed by controlling the cohesive and adhesive forces of CBD phases and AM particles. The electrochemical transport-relevant properties were further investigated under different conditions. Recently, Ngandjong et al. [23] developed a calendering model to evaluate the relationships between calendering pressure, microstructure and electrochemical performance. In their DEM model, Hertizan theory and simplified Johnson-Kendall-Roberts (JKR) model were used to describe the mechanical responses of particles, and they stated the simulation results matched well with experiments. Another piece of work of calendering model using DEM was recently reported by Schreiner et a. [24]. All the above demonstrate the potential to understand the calendering process and to optimise electrode microstructures by DEM. To successfully model the calendering process, appropriate contact mechanics models need to be considered to describe both the mechanical responses of AM particles and CBD phase. Furthermore, electrode structures used for simulations to date are stochastically generated by filling spherical particles with a controlled size distribution in a cubic volume, to achieve desired volume fractions. However, in a physical sample undergoing calendering the AM particles are spaced further apart, and the volume fractions of low-density CBD and pore phase need to be considered. The virtual structures in previous works with an incorrect calculation of volume fractions will therefore provide an unrealistic representation of the calendering process and can hamper the accurate performance comparison of simulation results with battery electrodes in reality.

In this contribution, an experimentally prepared cathode structure, characterised by X-ray tomography was used as an initial structure for a DEM calendering simulation. The tomography data collected by Ebner et al. [12] is used in this work. Simulated structures and relevant properties were compared with the corresponding experimentally characterised structures under different calendering pressures. Detailed force networks were calculated, and the anisotropy of electrode structures were analysed by using vectorial quantities, i.e. fabric tensor and stress tensor. Furthermore, the tortuosity factors under different conditions were calculated and compared with corresponding experimental results. Overall, this research demonstrates a promising way to quantitatively analyse the structural, mechanical and transport properties during electrode calendering by X-ray tomography and high fidelity DEM.

2. Methodology

2.1. Experimental data

In the research work proposed by Ebner et al. [12], the uncalendered structures and structures calendered at different pressures of approximately 300, 600, and 2000 bar were characterised by Synchrotron radiation X-ray tomography. The cathode structures were made of NMC 333 ($LiNi_{1/3}Mn_{1/3}Co_{1/3}O_2$), C65 carbon black and polyvinylidene fluoride (PVDF). In this work, structures with a mass ratio of NMC particles, carbon black and binder of 90:5:5 are considered. Samples were prepared by placing the electrodes in 15 mm diameter cylindrical molds, immersing them in epoxy resin and heating them at 55 °C for 24 h under vacuum. They were then milled to 0.7 mm width. Finally, the tomography scans with 0.37 μm voxel resolution were obtained.

In addition to the raw tomography data, the 3D reconstructed tomography scans were post processed using image segmentation algorithm, and the labelled particles with coordinates and volumes were offered by the database [12]. This information is directly used in this study.

2.2. DEM modelling method

By using DEM, the translational and rotational motion of an individual particle in the structure can be described by:

$$m^{\mathrm{k}}\frac{d\boldsymbol{v}^{\mathbf{k}}}{dt}=\boldsymbol{F}_{\mathrm{b}}^{\mathrm{k}}+\boldsymbol{F}_{\mathrm{p}}^{\mathrm{k}} \tag{1}$$

$$I^{\mathrm{k}}\frac{d\boldsymbol{\omega}^{\mathbf{k}}}{dt}=\boldsymbol{M}_{\mathrm{b}}^{\mathrm{k}}+\boldsymbol{M}_{\mathrm{p}}^{\mathrm{k}} \tag{2}$$

where m^{k} and I^{k} are the k^{th} particle mass and moment of inertia. $\boldsymbol{v}^{\mathbf{k}}$ and $\boldsymbol{\omega}^{\mathbf{k}}$ are the translational velocity and angular velocity. $\boldsymbol{F}_{\mathrm{b}}^{\mathrm{k}}$ and $\boldsymbol{M}_{\mathrm{b}}^{\mathrm{k}}$ are the bond force and bond torque that describe the CBD phase interactions in this work. $\boldsymbol{F}_{\mathrm{p}}^{\mathrm{k}}$ is the contact force of the neighbouring particles, and $\boldsymbol{M}_{\mathrm{p}}^{\mathrm{k}}$ is the contact torque that originate from the tangential contact force and rolling friction between neighbouring particles. For simplicity, the superscript k of an individual particle is omitted in the following sections.

2.2.1. The particle interactions

An Edinburgh elasto-plastic adhesive (EEPA) model is used to describe the interactions of micron sized AM particles [25].

The normal force $\boldsymbol{F}_{\mathrm{n,p}}$ is the sum of hysteretic spring force f_{hys} and damping force f_{nd} that can be calculated by:

$$\boldsymbol{F}_{\mathrm{n,p}}=\left(f_{\mathrm{hys}}+f_{\mathrm{nd}}\right)\boldsymbol{n} \tag{3}$$

where $\boldsymbol{n}$ is the unit normal vector from the contact point to the particle centre. The force-displacement relationship of f_{hys} can be expressed by:

$$f_{\mathrm{hys}}=\begin{cases} f_0+k_1\delta^n & \text{if } k_2\left(\delta^n-\delta_p^n\right)\geq k_1\delta^n \\ f_0+k_2\left(\delta^n-\delta_p^n\right) & \text{if } k_1\delta^n>k_2\left(\delta^n-\delta_p^n\right)>-k_{\mathrm{adh}}\delta^n \\ f_0-k_{\mathrm{adh}}\delta^n & \text{if } k_{\mathrm{adh}}\delta^n\geq k_2\left(\delta^n-\delta_p^n\right) \end{cases} \tag{4}$$

where f_0 is constant adhesion force, δ is total normal overlap, and δ_p^n is plastic overlap. k_1 is the loading stiffness, k_2 is the unloading stiffness, and k_{adh} is the adhesive stiffness, n is the non-linear index parameter.

The loading stiffness k_1 is calculated by:

$$k_1=\begin{cases} 2E^*R^* & \text{if } n=1 \\ \frac{4}{3}\sqrt{R^*}E^* & \text{if } n>1 \end{cases} \tag{5}$$

where E^* and R^* are the equivalent Young's modulus and radius. In this work, a non-linear slope exponent n=1.5 is chosen.

The contact plasticity ratio, λ_p is calculated using the following equation:

$$\lambda_p=\left(1-\frac{k_1}{k_2}\right) \tag{6}$$

The damping force f_{nd} can be calculated by:

$$f_{nd} = -\beta_n v_n \tag{7}$$

where v_n is the relative normal velocity, and β_n is the normal damping coefficient:

$$\beta_n = \sqrt{\frac{4m^* k_1}{1 + (\pi/\ln e)^2}} \tag{8}$$

where e is the coefficient of restitution.

The contact tangential force $\boldsymbol{F}_{t,p}$ is calculated by the sum of tangential spring force, $\boldsymbol{f}_{ts}$ and tangential damping force, $\boldsymbol{f}_{td}$:

$$\boldsymbol{F}_{t,p} = (\boldsymbol{f}_{ts} + \boldsymbol{f}_{td}) \tag{9}$$

The tangential spring force is expressed as:

$$\boldsymbol{f}_{ts} = \left(\boldsymbol{f}_{ts(n-1)} + \Delta \boldsymbol{f}_{ts}\right) \tag{10}$$

where $\boldsymbol{f}_{ts(n-1)}$ is the force of previous time step, and the incremental tangential force $\boldsymbol{\Delta f}_{ts}$ is calculated by:

$$\boldsymbol{\Delta f}_{ts} = -k_t \boldsymbol{v_t} \Delta t \tag{11}$$

where k_t is the tangential stiffness, $\boldsymbol{v_t}$ is the velocity in tangential direction, and Δt is the time step. The tangential stiffness can be calculated using the following equation:

$$k_t = \zeta_{tm} \begin{cases} k_1 \text{ if } n = 1 \\ 8G^* \sqrt{R^* \delta_n} \text{ if } n > 1 \end{cases} \tag{12}$$

where ζ_{tm} is the tangential stiffness multiplier, and G^* is the equivalent shear modulus. The tangential damping force $\boldsymbol{f}_{td}$ is calculated by:

$$\boldsymbol{f}_{td} = -\beta_t \boldsymbol{v_t} \tag{13}$$

The tangential damping coefficient β_t can be calculated by:

$$\beta_t = \sqrt{\frac{4m^* k_t}{1 + (\pi/\ln e)^2}} \tag{14}$$

The critical tangential force value f_{ct} is set equal to:

$$f_{ct} \le \mu \left| f_{hys} + k_{adh} \delta^n - f_0 \right| \tag{15}$$

where μ is the friction parameter. The total applied torque, $\boldsymbol{\eta_i}$ is calculated by:

$$\boldsymbol{\eta_i} = -\mu_r |f_{hys}| s_i \boldsymbol{\omega_i} \tag{16}$$

where μ_r is the rolling friction parameter, s_i is the distance from contact point to the particle center, and $\boldsymbol{\omega_i}$ is unit angular velocity at the contact point.

2.2.2. The binder phase interactions

The bond model firstly developed by Potyondy and Cundall [26] is used to describe the mechanical responses of the inter particle binder phase.

The normal force $\boldsymbol{F}_{n,b}$ can be expressed as a sum of the previous time step bond force $\boldsymbol{F}_{n(n-1),b}$ and the incremental tangential force $\Delta \boldsymbol{F}_{n,b}$:

$$\boldsymbol{F}_{n,b} = (\boldsymbol{F}_{n(n-1),b} + \Delta \boldsymbol{F}_{n,b}) \tag{17}$$

$$\boldsymbol{\Delta F}_{n,b} = -k_{n,b} \boldsymbol{v_{n,b}} \Delta t \tag{18}$$

where $k_{n,b}$ is the bond normal stiffness, and $\boldsymbol{v_{n,b}}$ is the velocity in normal direction.

The tangential spring force $\boldsymbol{F}_{t,b}$ is calculated as:

$$\boldsymbol{F}_{t,b} = (\boldsymbol{F}_{t(n-1),b} + \Delta \boldsymbol{F}_{t,b}) \tag{19}$$

$$\boldsymbol{\Delta F}_{t,b} = -k_{t,b} \boldsymbol{v_{t,b}} \Delta t \tag{20}$$

where $\boldsymbol{F}_{t(n-1),b}$ is the bond tangential force of the previous time step, $\Delta \boldsymbol{F}_{t,b}$ is the incremental tangential force, $k_{t,b}$ is the bond tangential stiffness, and $\boldsymbol{v_{t,b}}$ is the tangential velocity.

The bond tangential moments $\boldsymbol{M}_{t,b}$ and bond normal moments $\boldsymbol{M}_{n,b}$ calculated based on the incremental value from the previous time step can be expressed as:

$$\boldsymbol{M}_{t,b} = (\boldsymbol{M}_{t(n-1),b} + \Delta \boldsymbol{M}_{t,b}) \tag{21}$$

$$\boldsymbol{\Delta M}_{t,b} = -k_{t,b} A_b \boldsymbol{\omega_{t,b}} \Delta t I_b \tag{22}$$

$$\boldsymbol{M}_{n,b} = (\boldsymbol{M}_{n(n-1),b} + \Delta \boldsymbol{M}_{n,b}) \tag{23}$$

$$\boldsymbol{\Delta M}_{n,b} = -k_{n,b} A_b \boldsymbol{\omega_{n,b}} \Delta t J_b \tag{24}$$

where A_b is the bond cross sectional area, I_b and J_b are the moment of inertia and the polar moment inertia of the bond, $\boldsymbol{\omega_{t,b}}$ and $\boldsymbol{\omega_{n,b}}$ are relative angular velocities in tangential and normal directions.

The bond strength is calculated according to the beam theory as:

$$-\frac{\boldsymbol{F}_{n,b}}{A_b} + \frac{|\boldsymbol{M}_{t,b}| R_b}{I_b} < \sigma_n \tag{25}$$

$$\frac{|\boldsymbol{F}_{t,b}|}{A_b} + \frac{|\boldsymbol{M}_{n,b}| R_b}{I_b} < \sigma_t \tag{26}$$

where σ_n and σ_t are the tensile and shear strength of the bond, respectively.

2.3. Structure generation and DEM simulation setup

For the structure used in DEM simulation, a subdomain of an uncalendered structure containing a number of $N_p = 5106$ NMC 333 ($LiNi_{1/3}Mn_{1/3}Co_{1/3}O_2$) particles was chosen from the database [12] (Fig. 1 a). As illustrated in Fig. 1 (a), the structure with detailed particle position and diameter was imported into DEM simulations. Due to the high sphericity of NMC particles, spherical approximations were used for these particles. The particle size distribution by diameter is illustrated in Fig. 1 (c).

As shown in Fig. 1, inter-particle bonds were generated between AM particles to describe the mechanical response of CBD phase within electrode structures. The bonds are considered to be generated when the centre to centre distance of two neighbouring particles denoted by P_A and P_B meet the following criteria:

$$\|P_A - P_B\| \le \zeta_b \cdot (R_A + R_B) \tag{27}$$

where R_A and R_B are the particle radius. The bond radius is calculated as:

$$R_b = \lambda_b \cdot \min(R_A, R_B) \tag{28}$$

In this work, the two multipliers are set as $\zeta_b = 1.67$, $\lambda_b = 0.5$. The multipliers are chosen to ensure all the particles can be bonded together without unbonded particles. In addition, the multipliers were calculated to ensure the total bond volume is equivalent to the calculated CBD phase volume, according to the method in [19]. The inter-particle bonds were assigned to the particle assembly before compression, i.e., the multipliers were used to generate the initial bonded particle assembly, and they do not play a part during compression. The assigned inter-particle bonds show deformation/breakage during compression that correspond to the CBD phase mechanical properties in reality.

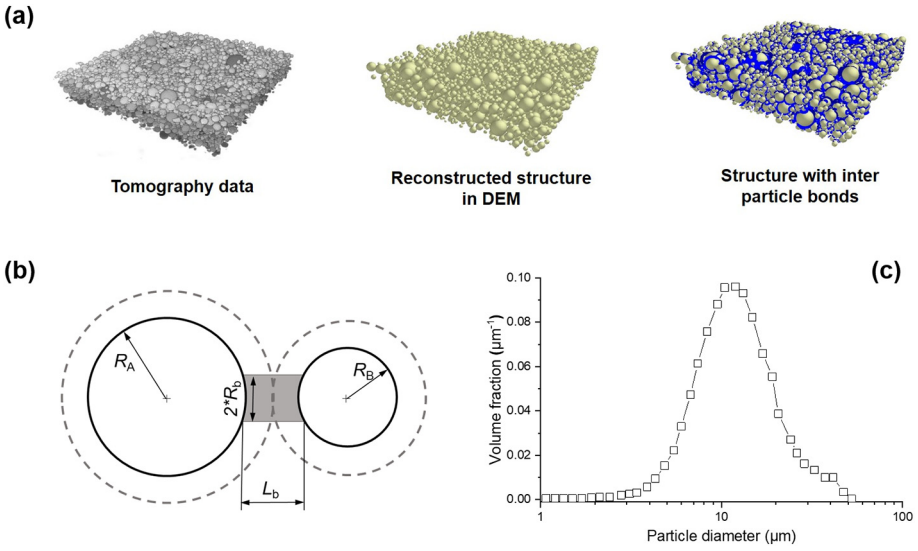

Fig. 1. Electrode structure generation used in DEM (a) tomography data processing (b) illustration of bond formation in DEM (c) active material (AM) particle size distribution [12].

An illustration of DEM simulation setup is shown in Fig. 2. Simulations were carried out using Altair EDEM 2021. The top plate is made of steel to represent the roller during calendering, and the bottom plate is aluminium to represent the current collector. Periodic boundaries were applied on the sides. To mimic the calendering process, the electrode structure was gradually compressed by moving the top plate with a constant speed of 0.01 m s^{-1}. The bond parameters are based on calibration results as illustrated in the following Fig. 4. The bond stiffness (k_b) values are 1.5×10^{14} N m^{-3}, and the bond strength (σ_n) values are 3×10^8 Pa. Other simulation parameters used in this work are listed in Table 1. Parameters were mainly taken from previous research work in this field. Mechanical properties of the top and bottom plate were from the EDEM material library.

2.4. Structure analysis method

After the DEM simulation, the electrode structures under different calendering levels were further analysed by calculating porosity and tortuosity factors.

2.4.1. Porosity analysis

Due to the soft particle model used in DEM simulations, the AM particles undergo deformations during calendering, and overlaps between AM particles can occur. Therefore, the accurate calculation of porosity is non-trivial and cannot be directly calculated using an analytical method. In this work, two statistical methods were considered to properly calculate the structure porosity, i.e. grid approach and Monte Carlo approach [37](Fig. 3).

(a) Grid approach.

As illustrated in Fig. 3 (a), a grid of simple cubic lattice points was generated in the calculated region. The porosity of the granular structure ε can be calculated by:

$$\varepsilon = 1 - N_{\text{Grid,Particle}} / N_{\text{Grid,Total}} \tag{29}$$

where $N_{\text{Grid,Particle}}$ is the number of grid points falling in the particle region, $N_{\text{Grid,Total}}$ is the total number of grid points in the whole region.

(b) Monte Carlo approach.

As for the Monte Carlo approach, a number of random points were generated in the calculated region (See Fig. 3 b). The porosity is calculated in a similar way as the grid method:

$$\varepsilon = 1 - N_{\text{MC,Particle}} / N_{\text{MC,Total}} \tag{30}$$

where $N_{\text{MC,Particle}}$ is the number of random points in the particle region, and $N_{\text{MC,Total}}$ is the number of random points in the whole region.

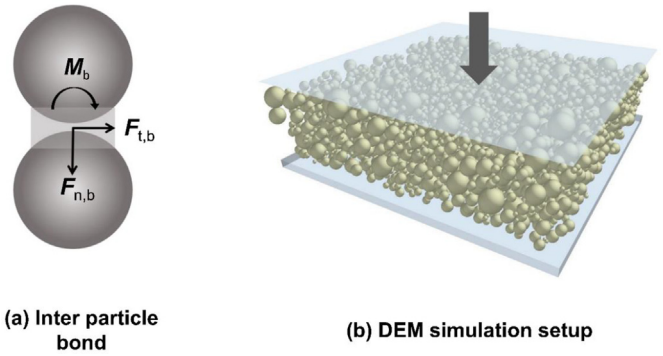

Fig. 2. DEM simulation setup of compression test.

Table 1
DEM simulation parameters used in this work [19,27] [16,20].

Description	Parameter	Value	Source
Particle Young's modulus (GPa)	E_{Par}	144	[19,27]
Particle density (kg m^{-3})	ρ_{Par}	4750	
Particle Poisson's ratio (−)	υ_{Par}	0.25	
Particle-particle static friction (−)	$\mu_{p,s}$	0.25	[16,20]
Particle-particle rolling friction (−)	$\mu_{p,r}$	0.01	
Coefficient of restitution (−)	e	0.5	
Plate Young's modulus (Steel) (GPa)	E_{St}	208	Material library
Plate density (Steel) (kg m^{-3})	ρ_{St}	7900	
Plate Poission's ratio (Steel) (−)	υ_{St}	0.3	
Plate Young's modulus (Aluminium) (GPa)	E_{Al}	68.9	
Plate density (Aluminium) (kg m^{-3})	ρ_{Al}	2700	
Plate Poission's ratio (Aluminium) (−)	υ_{Al}	0.3	

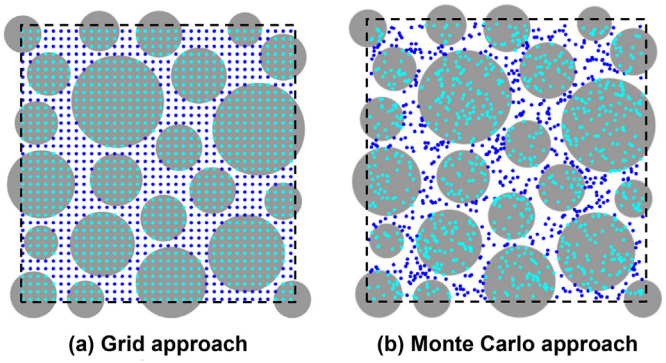

Fig. 3. Illustration of two porosity analysis methods (the lattice or random points in the particle region are colored in light green, while the points in the empty space are in blue).

To evaluate the reliability of these two methods, non-overlapping particles with 2–30 μm diameter were randomly generated in a 50 μm length cube. The porosity was analytically calculated by summing all the spherical particle volumes for comparison with the numerical predictions. As illustrated in Fig. 4, the relative errors of these two numerical methods were estimated considering different number of points. In general, the Monte Carlo approach can have a better prediction of porosity when using the same number of sampling points. Therefore, in the following the Monte Carlo approach is applied to calculate the porosity under different conditions. As each grid point can be treated as a voxel, the grid approach was used to generate voxelised volumes of particle structures, and then used for further tortuosity analysis and binder phase generation. A 0.5 μm pixel length was chosen to ensure the reliability of results. As shown in Fig. 4, when the number of points is larger than 1×10^6 (the corresponding pixel length is 0.5 um), the relative error of grid approach can fall below 2%. A further increase of the resolution to 0.1 um can slightly reduce the relative error to less than 1%, but the number of grid points is larger than 1×10^8 corresponding to a significant increased computation time.

2.4.2. Tortuosity analysis

The tortuosity factor τ has a significant impact on the transport properties of porous structures. It can be defined as:

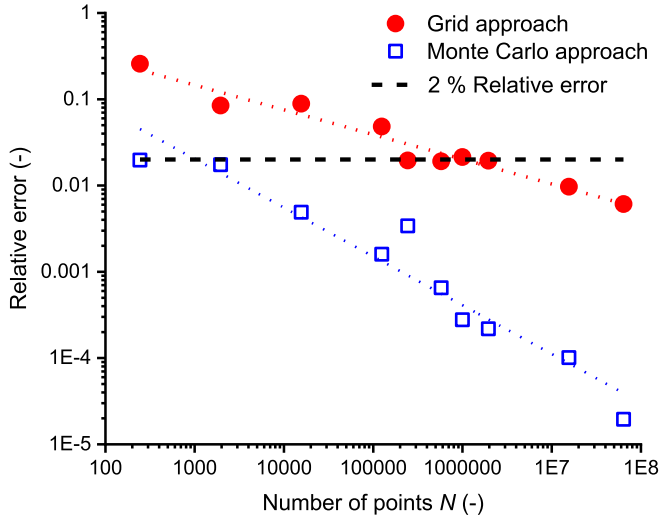

Fig. 4. Relative error analysis of porosity analysis for both grid and Monte Carlo methods.

$$D^{\text{eff}} = D\frac{\varepsilon}{\tau} \tag{31}$$

where D^{eff} is the diffusivity of the porous structure, D is the intrinsic diffusivity of the porous phase material. As illustrated in Fig. 5, the tortuosity can also be geometrically explained as:

$$\tau_{\text{geo}} = L_e/L_0 \tag{32}$$

where L_e is the actual length of the path through the porous structure, and L_0 is the straight-line length across the structure in the direction of flow (See Fig. 5). For all systems $\tau \geq 1$, and the flow paths are direct when $\tau = 1$. Various analytical, experimental and numerical methods have been proposed to calculate the tortuosity of porous structures [28–30]. In this work, the diffusion approach is considered. A MATLAB application *TauFactor*, based on numerically solving steady diffusive equations, was used for tortuosity analysis [29].

3. Results and discussion

3.1. Porosity comparison and voxelised structure generation

In DEM simulations, the electrode structures were compressed to achieve different calendering levels. The corresponding top plate pressures at different calendering levels were recorded. Four different compression pressures were used to generate electrode structures, as illustrated in Fig. 6. Using the Monte Carlo approach presented in Section 2.4.1, the porosities under different conditions were calculated and compared with the corresponding experimental results [12]. For making a quantitative comparison with the corresponding tomography scans, a proper definition and calculation of electrode structure porosity is necessary. In this section, the porosity $\varepsilon_{\text{Pore+binder}}$ was defined as the void volume fraction between AM particles considering both the pore and binder phase:

$$\varepsilon_{\text{Pore+binder}} = 1 - \varphi_{\text{Par}} \tag{33}$$

where φ_{Par} is the volume fraction of AM particles. As shown in Fig. 7, the porosity changes in DEM simulations are in good agreement with the corresponding tomography data at the respective stress levels. A slight deviation at the initial stage can be observed, and there are two likely primary reasons for this. Firstly, when using spherical approximations of AM particles in DEM simulations there is some volume loss. In addition, the experimental results are affected by the inhomogeneity of electrode structures in reality, which can be used to explain the unexpected variation tendency from 0 bar to 400 bar [12].

By using the grid approach presented in Section 2.4.1, the AM particle structures were converted to a stack of voxelised images. The 3D

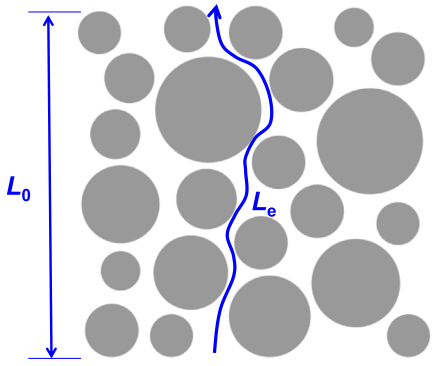

Fig. 5. Illustration of tortuosity within porous structures (tortuosity is a ratio of the actual path length L_e and the straight-line length L_0).

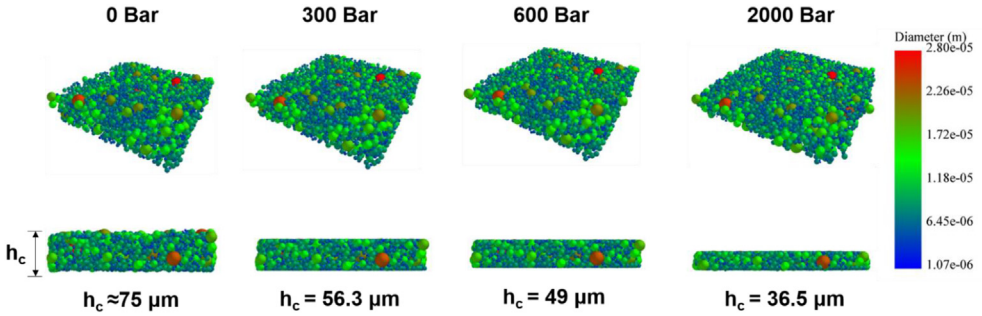

Fig. 6. Schematic of DEM simulation results under different compression pressures. The particle diameter is illustrated by changing colour from blue to green to red.

volume was chosen with a cross-section of 150 μm × 150 μm and it spans the entire thickness of the electrode (~30–70 μm). The voxelised 3D structures and corresponding 2D cross sectional images are illustrated in Fig. 8. It can be clearly observed from the 2D cross sectional images that the AM particle volume fraction increases with increased compression pressures. The generated voxelised 3D volumes are used for tortuosity analysis in the following section.

3.2. Stress and fabric tensor analysis

As the particles within the electrodes are connected by bond contacts, a complex network is formed. In this section, the contact force networks under different conditions were calculated from the particle contact data obtained by DEM simulations. Furthermore, vectorial quantities (i.e. contact normals $\boldsymbol{n}$ and contact forces) were analysed by using fabric tensor and stress tensor [31–33].

Fig. 9 illustrates the contact force network under different compression pressures. The force vectors at each particle contact pair are averaged and normalised as:

$$F_i = \sqrt{F_{x,i}^2 + F_{y,i}^2 + F_{z,i}^2}\; i = 1, 2 \cdots N_c \tag{34}$$

$$F_{i,\text{normalised}} = F_i / \max\left(F_1 \cdots F_{N_c}\right) i = 1, 2 \cdots N_c \tag{35}$$

where $F_{x,i}$, $F_{y,i}$ and $F_{z,i}$ are the contact force components of each particle contact in Cartesian coordinate system, N_c is the total number of particle contacts. The line weight in Fig. 9 is scaled by the magnitude of the normalised force $F_{i,\text{normalised}}$ at each contact. With increased calendering stress, the particle contact force becomes more obvious, and force chains are formed. Calendering affects the particle contact distributions, and more homogeneous inter-particle contacts can be generated with increased calendering levels as shown in Fig. 9.

The fabric tensor Φ_{ij} is used to study the directionality of particle contacts, which can be defined as the average of outer product of the contact normal $\boldsymbol{n}$ [31]:

$$\Phi_{ij} = \frac{1}{N_c} \sum_{\alpha=1}^{N_c} n_i n_j \tag{36}$$

where n_i and n_j are the projection of the unit contact normal $\boldsymbol{n}$ in Cartesian coordinate system. In this work, the contact normal $\boldsymbol{n}$ denotes the normal vectors of particle pairs, in which particles are either bonded or in contact with each other. The fabric tensor can be decomposed into isotropic and deviatoric part:

$$\Phi_{ij} = \frac{1}{3}\delta_{ij} + \Phi'_{ij} \tag{37}$$

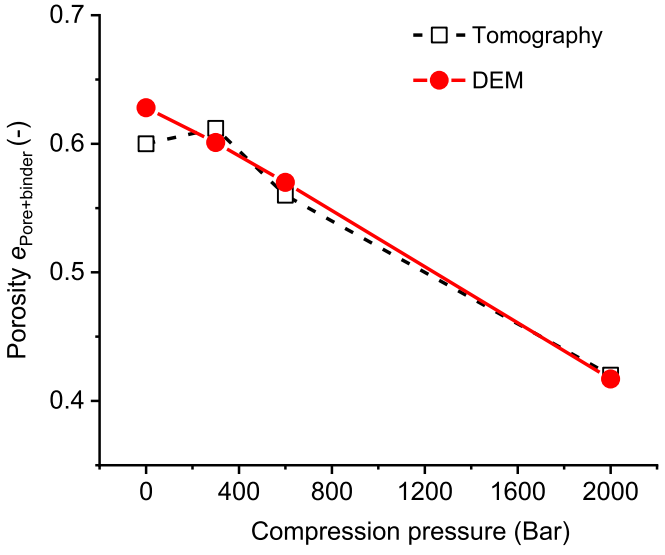

Fig. 7. Comparison of porosity $\varepsilon_{\text{Pore+binder}}$ under different compression pressures, the tomography data is from Ebner et al. [12].

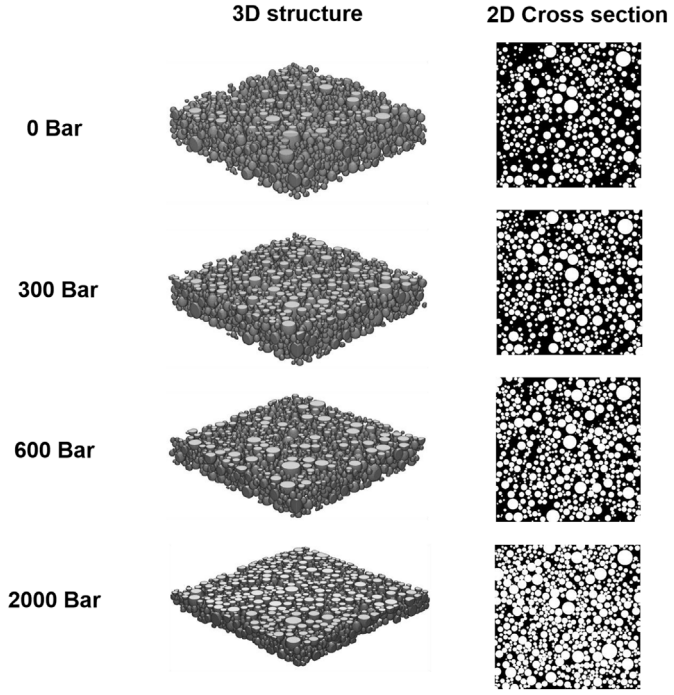

Fig. 8. Voxelised 3D electrode structures and 2D cross sections from DEM simulations under different compression pressures (In the 2D cross section, the white voxels are AM particles, and black voxels are voids).

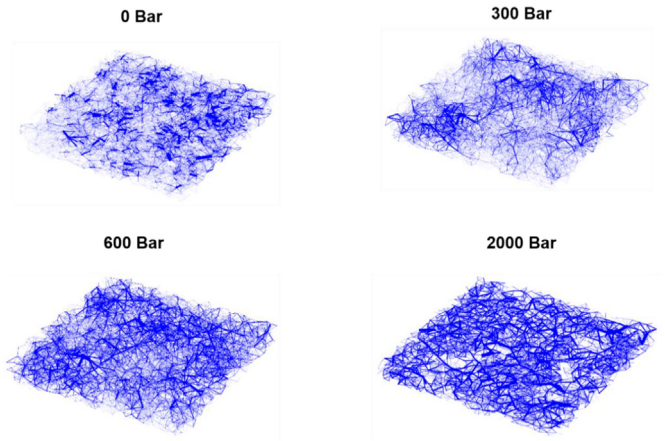

Fig. 9. Contact force network under different compression pressures.

where δ_{ij} is the Kroenecker delta, and Φ'_{ij} is the deviatoric part. The particle contact information under different conditions is analysed and the diagonal components of deviatoric part Φ'_{ij} are shown in Fig. 10. In Fig. 10, Φ'_{xx} and Φ'_{yy} represent the direction parallel to the current collector, and Φ'_{zz} is the normal direction of compression. It can be observed that Φ'_{xx} and Φ'_{yy} increase gradually with increased compression pressure. The Φ'_{zz} in the normal direction shows a contrary tendency as it decreases from −0.018 to −0.04 with the increased compression pressures. As the Φ'_{xx} and Φ'_{yy} indicate the homogeneity of particle contacts through the *x*-*y* plane, they show very similar value range and variation trends. However, it is interesting to see that Φ'_{xx} is slightly higher than Φ'_{yy} for all structures under different compression pressures. This is possibly because of the particle contact difference from the original electrode structures. It is worth to investigate if this difference can be related to the manufacturing process in reality. As illustrated in Fig. 10, the diagonal components of deviatoric part Φ'_{ij} and the calendering conditions are strongly related. In future it is also worthwhile to investigate the effect of the particle size distribution on the particle contacts and corresponding Φ'_{ij}.

The stress tensor σ_{ij} within a representative elementary volume V can be described as [33,34]:

$$\sigma_{ij} = \frac{1}{2V}\sum_{\alpha=1}^{N_c}\left(r_{1i}F_{1j} + r_{2i}F_{2j}\right) \tag{38}$$

where r_{1i} and r_{2i} are the relative positions of the two particles in a pair, and F_{1j} and F_{2j} are the interaction forces acting on each other. The calculated results of diagonal components are presented in Fig. 11. The stress within the electrodes increases with increased calendering levels. σ_{xx} and σ_{yy} are approximately the same, and σ_{zz} in the normal direction is higher for all calendering conditions. The fabric tensor and corresponding stress indicate the topological and anisotropic features of particle contacts within electrode structures that may affect the electrode performance considering different directions.

3.3. Tortuosity analysis

The tortuosity factor can represent the lithium ion transport feasibility in the electrolyte phase. It is an important property as it limits the maximum charge/discharge rate for battery electrodes [28]. In this work, the average tortuosity factor $\tau_{\mathrm{Pore+binder}}$ in which the porous phase containing both the pore and binder were calculated and presented in Fig. 7. In this figure, the average tortuosity factors of DEM simulated structures are compared with the results from X-ray tomography under the same stress levels. Representative volume analysis results of the tortuosity factor $\tau_{\mathrm{Pore+binder}}$ from 20% to 100% volume fractions of the electrode structure shown that the varied volume fractions have minimal effects (less than 5%) on the tortuosity factor values. As illustrated in Fig. 12, the tortuosity factor increases with the increased calendering pressures. The tortuosity factor from DEM simulations shows a very similar variation tendency with the results from the 3D structures characterised by X-ray tomography [12]. The slight discrepancy may be due to plastic deformation and breakage of AM particles in calendering experiments, which was not captured in the simulation results here [12]. Another cause for discrepancy reason is the non-uniform, non-spherical shape of AM particles, which cannot be captured by current DEM simulations.

The reconstructed structure and relative properties, i.e. $\varepsilon_{\mathrm{Pore+binder}}$ and $\tau_{\mathrm{Pore+binder}}$ only contain the geometrical features of AM particles. As the CBD phase is not visible from the tomography data, a binder generation algorithm was developed to evaluate the effect of binder phase on tortuosity factors. Pendular ring shaped binder phases were generated between AM particles using a level-set method recently proposed by Trembacki et al. [35]. The binder phase ψ_{Binder} can be defined as:

$$\psi_{\mathrm{Binder}} = min\left[(\psi_{\mathrm{P,i}} + O)*\left(\psi_{\mathrm{P,j}} + O\right) - S, \cdots, \left(\psi_{\mathrm{P,N_p}} + O\right)*\left(\psi_{\mathrm{P,N_p}} + O\right) - S\right], i \neq j \tag{39}$$

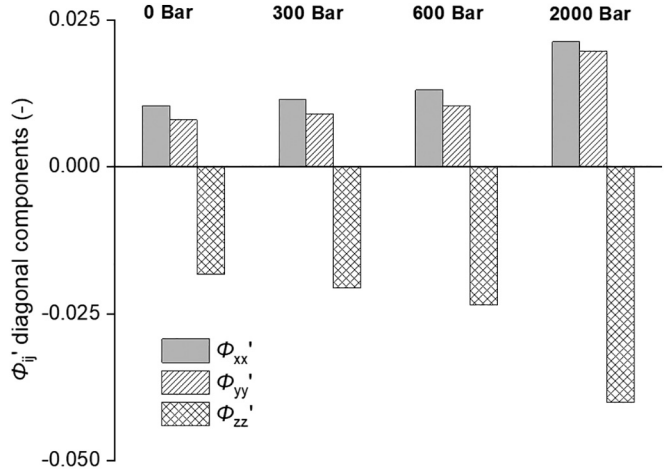

Fig. 10. Diagonal components of deviatoric part Φ_{ij}' of the fabric tensor under different compression pressures.

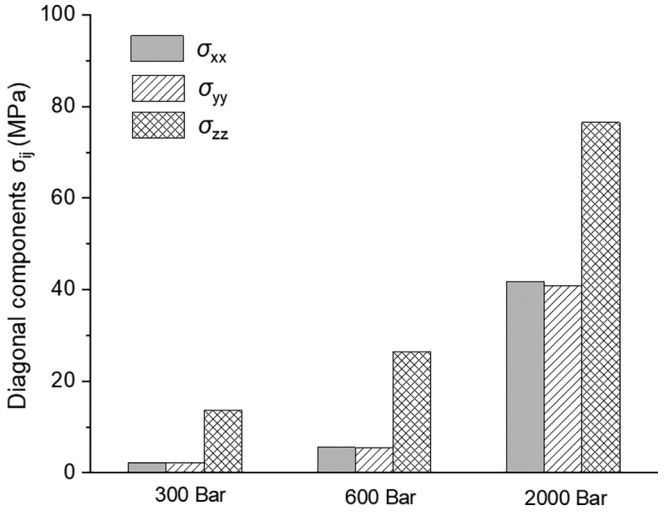

Fig. 11. Diagonal components of the stress tensor σ_{ij} for the calendered electrodes under different compression pressures.

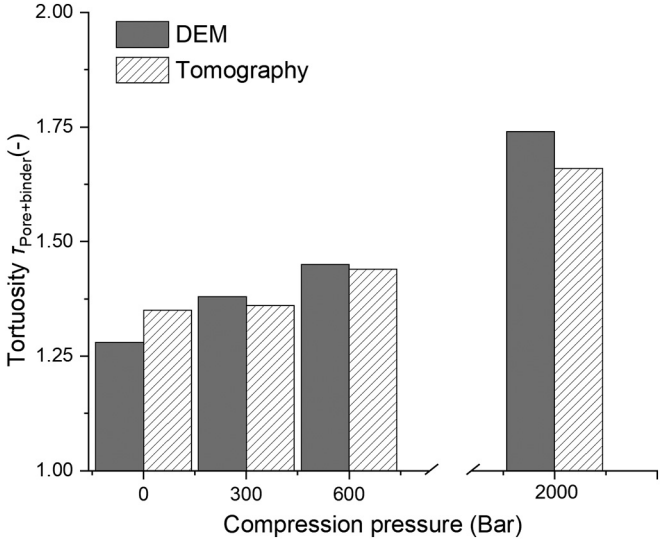

Fig. 12. Comparison of average tortuosity factor $\tau_{Pore+binder}$ under different compression pressures.

Table 2
Values of S parameters for binder phase generation, and corresponding AM particle volume fraction φ_{Par} and porosity ε_{Pore}.

	0 Bar	300 Bar	600 Bar	2000 Bar
S	998	976.5	966.5	976
φ_{Par}	0.372	0.399	0.43	0.583
ε_{Pore}	0.525	0.49	0.45	0.255

where $\psi_{P,i}$ is the level set of an individual particle, N_p is the total particle number. The binder phase is generated for all particle pairs with the particle number index ranges from 1 to N_p. The parameter O and S in the above equation are used to control the binder morphology and amount respectively. The particle level sets are shrunk by using offset O (shape), and then grown by the offset S (size) preferentially between two neighbour particles. In this work, the shape parameter $O = 30$ μm, while the size parameter S is tuned to achieve different prescribed electrode porosities ε_{Pore}. The electrode porosity ε_{Pore} in which the porous phase containing only pores can be theoretically estimated by:

$$\varepsilon_{Pore} = 1-\varphi_{Par}-\varphi_{Par}\cdot x/(100-2x)\cdot(\rho_{Par}/\rho_{CB}+\rho_{Par}/\rho_{PVDF}) \quad (40)$$

where the mass ratio $x = 5$ (in wt%), NMC density $\rho_{Par} = 4.7\ gcm^{-3}$, carbon black density $\rho_{CB} = 2\ gcm^{-3}$ and binder density $\rho_{PVDF} = 1.78\ gcm^{-3}$ [12]. Detailed S parameters, and the corresponding particle volume fraction φ_{Par} and porosity ε_{Pore} are listed in Table 2.

A 2D slice parallel to the through plane direction is illustrated in Fig. 13 (a). The generated pendular ring shaped binder phase can be observed in this figure. The corresponding potential distributions of the diffusing species in the porous phase are calculated from diffusion equations and illustrated in Fig. 13 (b). The corresponding tortuosity factors are plotted in Fig. 13 (c). When considering the effect of binder phase, the calculated tortuosity factor τ_{pore} is higher than the tortuosity factor $\tau_{Pore+binder}$ containing both the pore and binder in the porous phase. Traditionally, the Bruggeman effective medium equation $\tau = \varepsilon^{-0.5}$ is used to describe the tortuosity of electrode structures [36]. In this work, the data of τ_{Pore} and $\tau_{Pore+binder}$ are fitted by a generalized equation $\tau = a\varepsilon^b$. As shown in Fig. 13(c), $\tau_{Pore+binder}$ ($\tau_{Pore+binder} = 1.02\varepsilon^{-0.53}_{Pore+binder}$) has a very consistent tendency with the classical Bruggeman equation. This is reasonable as the structures generated from DEM simulations are mono-sized spherical particle packing. After considering the effect of binder phase, the data is fitted as $\tau_{Pore} = 0.885\varepsilon^{-1.068}$. The fitting curve agrees with the data from experiments using 90% AM mass loadings [28]. There is some slight discrepancy as the current simulation results cannot resolve the detailed nano-sized pores of binder phase. As the results of blue and red curves in Fig. 13 (c) are based on the same AM particle structures, the main difference of these two curves is from the absence/presence of binder phase. For the first time the results show the tortuosity of a calendered electrode can be predicted by combining DEM simulation and a binder phase generation algorithm. In future, it is useful to investigate the effect of AM particle size distribution and binder phase volumes via artificially generated electrode structures. The generated microstructures under different calendering conditions can be further used to electrochemical analysis of lithium ion batteries.

4. Conclusions

In this work, DEM simulation was used to study the structure and corresponding properties of lithium ion battery electrodes under different calendering conditions. The mechanical properties of AM particles and binder phase were described by an EEPA model and a bond model. Using an uncalendered electrode structure characterised by X-ray tomography as an initial structure, the DEM simulation results were compared with experimental results under same calendering pressures. The main conclusions are:

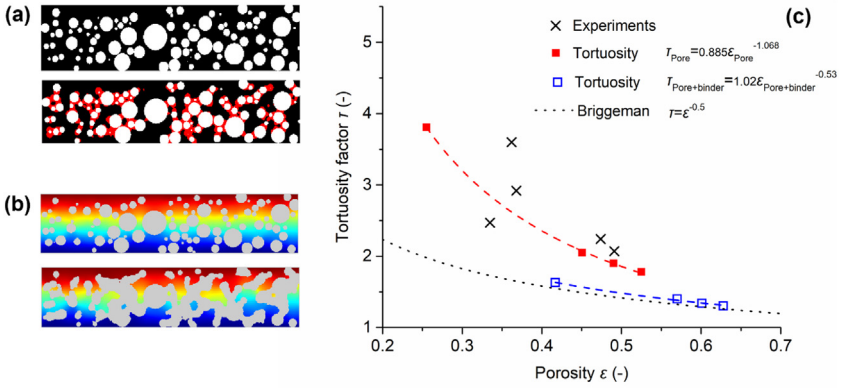

Fig. 13. Tortuosity factor with/without binder phase (a) 2D visualisation of electrode structure parallel to the through plane direction, the binder phase is colored in red. (b) Normalised potential distribution without/with binder phase. (c) Tortuosity factor τ plotted as a function of porosity.

1. The porosity of electrode structures was accurately defined by considering different phases. Two statistical methods, i.e. Monte Carlo approach and grid approach were used to accurately calculate the porosity $\varepsilon_{\text{Pore+binder}}$ of simulated structures and generate voxelised electrode structure. The porosity $\varepsilon_{\text{Pore+binder}}$ calculated from DEM simulations shows good agreement with the corresponding AM particle structures experimentally obtained from X-ray tomography.
2. The contact force networks under different conditions were calculated by using data from DEM simulations. Following this the fabric tensor and stress tensor were analysed. From a point of quantitative view, the simulation results reveal the inhomogeneous stress distribution and anisotropic properties of electrode structures under different calendering conditions.
3. The calculated tortuosity factors $\tau_{\text{pore+binder}}$ from DEM are in agreement with the results calculated from corresponding tomography structures. By generating the binder phase using a level set method, tthe tortuosity factors τ_{pore} considering binder phase effect were calculated. The results show similar tendency with the experimental data of 90% AM mass loading structures.

This work demonstrates, for the first time, the feasibility of combining X-ray tomography and DEM to quantitatively analyse electrode structure evolution during calendering. This approach is useful to digitalize electrode design, as it incorporates the realistic microstructure and material properties. The high-fidelity particle scale information can be obtained under each incremental calendering step, which could be useful to optimise electrode structures with desired mechanical and transport properties. It is important to emphasise that spherical particle approximations were used in this work, and the effect of particle fracture is not considered. These limitations may affect model prediction, especially under high calendering pressures. There is opportunity for future work to consider non-spherical particle shapes and CBD phase distribution resolved by tomography in DEM simulations.

Nomenclature

A_b	Bond cross sectional area, m^2
a	Constant, —
b	Constant, —
D	The intrinsic diffusivity, $m^2\ s^{-1}$
D^{eff}	The diffusivity of the porous structure, $m^2\ s^{-1}$
E^*	Equivalent Young's modulus, MPa
E_{Par}	Particle Young's modulus, MPa
E_{St} / E_{Al}	Plate Young's modulus, MPa
e	Coefficient of restitution, —
$\boldsymbol{F}$	Contact force, N
$F_{x,i}, F_{y,i}, F_{z,i}$	The i^{th} contact force components in Cartesian coordinate system, N
$F_{\text{i,normalised}}$	The i^{th} normalised contact force, N
$\boldsymbol{F}_{\text{n,p}}, \boldsymbol{F}_{\text{n,b}}$	Particle/bond normal force, N
$\boldsymbol{F}_{\text{t,p}}, \boldsymbol{F}_{\text{t,b}}$	Particle/bond tangential force, N
f_{ct}	Critical tangential force, N
f_{hys}	Hysteretic spring force, N
f_{nd}	Damping force, N
f_{ts}	Tangential spring force, N
f_{td}	Tangential damping force, N
f_0	Constant adhesion force, N
G^*	Equivalent shear modulus, MPa
h_c	Electrode thickness, m
I_b	Bond moment of inertia, kg m^2
J_b	Bond polar moment of inertia, m^4
k_1	Loading stiffness, N m^{-1}
k_2	Unloading stiffness, N m^{-1}
k_{adh}	Adhesive stiffness, N m^{-1}
k_t	Tangential stiffness, N m^{-1}
$k_{n,b}$	Bond normal stiffness, N m^{-1}
$k_{t,b}$	Bond tangential stiffness, N m^{-1}
L_b	Bond length, m
L_e	Actual path length through the porous structure, m
L_0	Straight-line length across the structure, m
M	Torque, N.m
$\boldsymbol{M}_{\text{n,b}}$	Bond normal moment, N m
$\boldsymbol{M}_{\text{t,b}}$	Bond tangential moment, N m
m	Mass, kg
N_c	The total number of particle contacts, —
N_p	The total number pf particles, —
$N_{\text{Grid,Particle}}$	The number of grid points in the particle region, —
$N_{\text{Grid,Total}}$	The total number of grid points in the whole region, —
$N_{\text{MC,Particle}}$	The number of random points in the particle region, —
$N_{\text{MC,Total}}$	The total number of random points in the whole region, —
$\boldsymbol{n}$	Unit contact normal vector, —
n_i, n_j	Projection of the unit contact normal, —
O	Binder shape parameter, μm
R^*	Equivalent radius, m
R_A, R_B	Particle radius, m
R_b	Bond radius, m
r_{1i}, r_{2i}	Relative positions of two particles in a pair, —
S	Binder size parameter, μm^2
s_i	Distance from contact point to the particle center, m
t	Time, s
V	Representative elementary volume, m^3
$\boldsymbol{v}$	Velocity, m s^{-1}
v_n	Relative normal velocity, m s^{-1}
v_t	Relative tangential velocity, m s^{-1}
x	Mass ratio, wt%

Greek symbols

β_n	Normal damping coefficient, —
β_t	Tangential damping coefficient, —
δ	Normal overlap, m
ε	Porosity, —
$\varepsilon_{\text{Pore+binder}}$	Electrode porosity (Porous phase containing both the pore and the binder), —
$\varepsilon_{\text{Pore}}$	Electrode porosity (Porous phase containing only pores), —
ζ_b	Bond length multiplier, —
ζ_{tm}	Tangential stiffness multiplier, —
λ_b	Bond radius multiplier, —
λ_p	Plasticity ratio, —
μ_s	Friction coefficient,-
μ_r	Rolling friction coefficient,-
ν_{Par}	Particle poission's ratio,-
ν_{St} / ν_{Al}	Plate poission's ratio,-
ρ_{Par}	Particle density, $m^3\ kg^{-1}$
ρ_{CB}	Carbon black density, $m^3\ kg^{-1}$
ρ_{PVDF}	Binder density, $m^3\ kg^{-1}$
ρ_{St} / ρ_{Al}	Plate density, $m^3\ kg^{-1}$
σ_n	Tensile bond strength, MPa
σ_t	Shear bond strength, MPa
σ_{ij}	Stress tensor, MPa
τ_{geo}	Geometric tortuosity, —
$\tau_{\text{Pore+binder}}$	Tortuosity factor (Porous phase containing both the pore and binder), —
τ_{Pore}	Tortuosity factor (Porous phase containing only pores), —
Φ_{ij}	Fabric tensor, —
Φ'_{ij}	Deviatoric part of fabric tensor, —
φ_{Par}	Volume fraction of AM particles, —
Ψ_{Binder}	Level set of binder phase, —
$\Psi_{\text{P,i}}$	Level set of an individual particle, —
$\boldsymbol{\omega}$	Angular velocity, s^{-1}

CRediT authorship contribution statement

Ruihuan Ge: Writing – original draft, Methodology, Software. **Denis Cumming:** Data curation, Supervision, Writing – review & editing. **Rachel Smith:** Conceptualization, Supervision, Writing – review & editing.

Declaration of Competing Interest

The authors declare that they have no known competing financial interests or personal relationships that could have appeared to influence the work reported in this paper.

Acknowledgments

The authors would like to acknowledge the financial support from Faraday Institution NEXTRODE project (Grant Number: FIRG015). They would also like to acknowledge Dr. Marina Sousani from Altair EDEM® for discussing the DEM simulations. The support of Altair EDEM® for providing EDEM licences is greatly acknowledged.

References

[1] O. Gröger, H.A. Gasteiger, J.-P. Suchsland, Electromobility: batteries or fuel cells? J. Electrochem. Soc. 162 (14) (2015) A2605.
[2] A. Kwade, W. Haselrieder, R. Leithoff, A. Modlinger, F. Dietrich, K. Droeder, Current status and challenges for automotive battery production technologies, Nat. Energy 3 (4) (2018) 290–300.
[3] X. Lu, A. Bertei, D.P. Finegan, C. Tan, S.R. Daemi, J.S. Weaving, K.B. O'Regan, T.M. Heenan, G. Hinds, E. Kendrick, 3D microstructure design of lithium-ion battery electrodes assisted by X-ray nano-computed tomography and modelling, Nat. Commun. 11 (1) (2020) 1–13.
[4] G. Lenze, F. Röder, H. Bockholt, W. Haselrieder, A. Kwade, U. Krewer, Simulation-supported analysis of calendering impacts on the performance of lithium-ion-batteries, J. Electrochem. Soc. 164 (6) (2017) A1223.
[5] X. Lu, S.R. Daemi, A. Bertei, M.D. Kok, K.B. O'Regan, L. Rasha, J. Park, G. Hinds, E. Kendrick, D.J. Brett, Microstructural evolution of battery electrodes during calendering, Joule 4 (12) (2020) 2746–2768.
[6] C. Meyer, H. Bockholt, W. Haselrieder, A. Kwade, Characterization of the calendering process for compaction of electrodes for lithium-ion batteries, J. Mater. Process. Technol. 249 (2017) 172–178.
[7] D. Schreiner, M. Oguntke, T. Günther, G. Reinhart, Modelling of the calendering process of NMC-622 cathodes in battery production analyzing machine/material–process–structure correlations, Energy Technol. 7 (11) (2019) 1900840.
[8] E.N. Primo, M. Chouchane, M. Touzin, P. Vázquez, A.A. Franco, Understanding the calendering processability of Li (Ni0. 33Mn0. 33Co0. 33) O2-based cathodes, J. Power Sources 488 (2021) 229361.
[9] B.G. Westphal, N. Mainusch, C. Meyer, W. Haselrieder, M. Indrikova, P. Titscher, H. Bockholt, W. Viöl, A. Kwade, Influence of high intensive dry mixing and calendering on relative electrode resistivity determined via an advanced two point approach, J. Energy Stor. 11 (2017) 76–85.
[10] W. Haselrieder, S. Ivanov, D.K. Christen, H. Bockholt, A. Kwade, Impact of the calendering process on the interfacial structure and the related electrochemical performance of secondary lithium-ion batteries, ECS Trans. 50 (26) (2013) 59.
[11] G. Lenze, H. Bockholt, C. Schilcher, L. Froböse, D. Jansen, U. Krewer, A. Kwade, Impacts of variations in manufacturing parameters on performance of lithium-ion-batteries, J. Electrochem. Soc. 165 (2) (2018) A314.
[12] M. Ebner, F. Geldmacher, F. Marone, M. Stampanoni, V. Wood, X-ray tomography of porous, transition metal oxide based lithium ion battery electrodes, Adv. Energy Mater. 3 (7) (2013) 845–850.
[13] S.R. Daemi, C. Tan, T. Volkenandt, S.J. Cooper, A. Palacios-Padros, J. Cookson, D.J. Brett, P.R. Shearing, Visualizing the carbon binder phase of battery electrodes in three dimensions, ACS Appl. Energy Mater. 1 (8) (2018) 3702–3710.
[14] L. Zielke, T. Hutzenlaub, D.R. Wheeler, C.W. Chao, I. Manke, A. Hilger, N. Paust, R. Zengerle, S. Thiele, Three-phase multiscale modeling of a LiCoO2 cathode: combining the advantages of FIB–SEM imaging and x-ray tomography, Adv. Energy Mater. 5 (5) (2015) 1401612.
[15] L. Zielke, T. Hutzenlaub, D.R. Wheeler, I. Manke, T. Arlt, N. Paust, R. Zengerle, S. Thiele, A combination of x-ray tomography and carbon binder modeling: reconstructing the three phases of LiCoO2 Li-ion battery cathodes, Adv. Energy Mater. 4 (8) (2014) 1301617.
[16] R. Ge, M. Ghadiri, T. Bonakdar, Q. Zheng, Z. Zhou, I. Larson, K. Hapgood, Deformation of 3D printed agglomerates: multiscale experimental tests and DEM simulation, Chem. Eng. Sci. 217 (2020) 115526.
[17] R. Ge, L. Wang, Z. Zhou, DEM analysis of compression breakage of 3D printed agglomerates with different structures, Powder Technol. 356 (2019) 1045–1058.
[18] M.M. Forouzan, C.-W. Chao, D. Bustamante, B.A. Mazzeo, D.R. Wheeler, Experiment and simulation of the fabrication process of lithium-ion battery cathodes for determining microstructure and mechanical properties, J. Power Sources 312 (2016) 172–183.
[19] C.S. Giménez, B. Finke, C. Schilde, L. Froböse, A. Kwade, Numerical simulation of the behavior of lithium-ion battery electrodes during the calendaring process via the discrete element method, Powder Technol. 349 (2019) 1–11.
[20] A. Stershic, S. Simunovic, J. Nanda, Modeling the evolution of lithium-ion particle contact distributions using a fabric tensor approach, J. Power Sources 297 (2015) 540–550.
[21] C. Sangrós Giménez, C. Schilde, L. Froböse, S. Ivanov, A. Kwade, Mechanical, electrical, and ionic behavior of lithium-ion battery electrodes via discrete element method simulations, Energy Technol. 8 (2) (2020) 1900180.
[22] I. Srivastava, D.S. Bolintineanu, J.B. Lechman, S.A. Roberts, Controlling binder adhesion to impact electrode mesostructures and transport, ACS Appl. Mater. Interfaces 12 (31) (2020) 34919–34930.
[23] A.C. Ngandjong, T. Lombardo, E.N. Primo, M. Chouchane, A. Shodiev, O. Arcelus, A.A. Franco, Investigating electrode calendering and its impact on electrochemical performance by means of a new discrete element method model: towards a digital twin of Li-Ion battery manufacturing, J. Power Sources 485 (2021) 229320.
[24] D. Schreiner, A. Klinger, G. Reinhart, Modeling of the calendering process for lithium-ion batteries with DEM simulation, Proc. CIRP 93 (2020) 149–155.
[25] S.C. Thakur, H. Ahmadian, J. Sun, J.Y. Ooi, An experimental and numerical study of packing, compression, and caking behaviour of detergent powders, Particuology 12 (2014) 2–12.
[26] D.O. Potyondy, P. Cundall, A bonded-particle model for rock, Int. J. Rock Mech. Min. Sci. 41 (8) (2004) 1329–1364.
[27] L.S. de Vasconcelos, R. Xu, J. Li, K. Zhao, Grid indentation analysis of mechanical properties of composite electrodes in Li-ion batteries, Extreme Mech. Lett. 9 (2016) 495–502.
[28] F.L. Usseglio-Viretta, A. Colclasure, A.N. Mistry, K.P.Y. Claver, F. Pouraghajan, D.P. Finegan, T.M. Heenan, D. Abraham, P.P. Mukherjee, D. Wheeler, Resolving the discrepancy in tortuosity factor estimation for Li-ion battery electrodes through micro-macro modeling and experiment, J. Electrochem. Soc. 165 (14) (2018) A3403.
[29] S. Cooper, A. Bertei, P. Shearing, J. Kilner, N. Brandon, TauFactor: an open-source application for calculating tortuosity factors from tomographic data, SoftwareX 5 (2016) 203–210.
[30] R.I. Al-Raoush, I.T. Madhoun, TORT3D: a MATLAB code to compute geometric tortuosity from 3D images of unconsolidated porous media, Powder Technol. 320 (2017) 99–107.
[31] K. Ken-Ichi, Distribution of directional data and fabric tensors, Int. J. Eng. Sci. 22 (2) (1984) 149–164.
[32] M. Satake, Fabric Tensor in Granular Materials, 1982.
[33] J. Christoffersen, M.M. Mehrabadi, S. Nemat-Nasser, A Micromechanical Description of Granular Material Behavior, 1981.
[34] M.M. Mehrabadi, S. Nemat-Nasser, M. Oda, On statistical description of stress and fabric in granular materials, Int. J. Numer. Anal. Methods Geomech. 6 (1) (1982) 95–108.
[35] B.L. Trembacki, D.R. Noble, M.E. Ferraro, S.A. Roberts, Mesoscale effects of composition and calendering in lithium-ion battery composite electrodes, J. Electrochem. Energy Convers. Stor. 17 (4) (2020).
[36] B. Tjaden, S.J. Cooper, D.J. Brett, D. Kramer, P.R. Shearing, On the origin and application of the Bruggeman correlation for analysing transport phenomena in electrochemical systems, Curr. Opin. Chem. Eng. 12 (2016) 44–51.
[37] Luca Orefice, Johannes G. Khinast, Deformable and breakable DEM particle clusters for modelling compression of plastic and brittle porous materials — Model and structure properties, Powder Technology 368 (2020) 90–104, https://doi.org/10.1016/j.powtec.2020.04.035.